

Probing the Meissner effect in pressurized bilayer nickelate superconductors using diamond quantum sensors

Junyan Wen^{1,2†}, Yue Xu^{1,2†}, Gang Wang^{1,2†}, Ze-Xu He^{1,2}, Yang Chen¹, Ningning Wang^{1,2}, Tenglong Lu¹, Xiaoli Ma^{1,2}, Feng Jin^{1,2}, Liucheng Chen¹, Miao Liu¹, Jing-Wei Fan³, Xiaobing Liu⁴, Xin-Yu Pan^{1,2,5}, Gang-Qin Liu^{1,2,5*}, Jinguang Cheng^{1,2*}, Xiaohui Yu^{1,2*}

¹*Beijing National Laboratory for Condensed Matter Physics and Institute of Physics, Chinese Academy of Sciences, Beijing 100190, China*

²*School of Physical Sciences, University of Chinese Academy of Sciences, Beijing 100190, China*

³*Department of Physics, Hefei University of Technology, Hefei, Anhui 230009, China*

⁴*Laboratory of High Pressure Physics and Material Science, School of Physics and Physical Engineering, Qufu Normal University, Qufu, Shandong Province, 273165, China*

⁵*CAS Center of Excellence in Topological Quantum Computation, Beijing 100190, China*

† These authors contribute equally to this work.

*Corresponding authors: gqliu@iphy.ac.cn; jgcheng@iphy.ac.cn; yuxh@iphy.ac.cn

Abstract

Recent reports on the signatures of high-temperature superconductivity with a critical temperature T_c close to 80 K have triggered great research interest and extensive follow-up studies¹⁻⁸. Although zero-resistance state has been successfully achieved under improved hydrostatic pressure conditions^{2,3,9}, there is no clear evidence of superconducting diamagnetism in pressurized $\text{La}_3\text{Ni}_2\text{O}_{7-\delta}$ due to the low superconducting volume fraction and limited magnetic measurement techniques under high pressure conditions¹⁰. Here, using shallow nitrogen-vacancy centers implanted on the culet of diamond anvils as in-situ quantum sensors, we observe convincing evidence for the Meissner effect in polycrystalline samples $\text{La}_3\text{Ni}_2\text{O}_{7-\delta}$ and $\text{La}_2\text{PrNi}_2\text{O}_7$: the magnetic field expulsion during both field cooling and field warming processes. The correlated measurements of Raman spectra and NV-based magnetic imaging indicate an incomplete structural transformation related to the displacement of oxygen ions emerging in the non-superconducting region. Furthermore, comparative experiments on different pressure transmitting media (silicone oil and KBr) and nickelates ($\text{La}_3\text{Ni}_2\text{O}_{7-\delta}$ and $\text{La}_2\text{PrNi}_2\text{O}_7$) reveal that an improved hydrostatic pressure conditions and the substitution of La by Pr in $\text{La}_3\text{Ni}_2\text{O}_{7-\delta}$ can dramatically increase the superconductivity. Our work clarifies the controversy about the Meissner

effect of bilayer nickelate and contributes to a deeper understanding of the mechanism of nickelate high-temperature superconductors.

Introduction

Since superconductivity has been observed in thin $\text{Nd}_{1-x}\text{Sr}_x\text{NiO}_2$ films, the study of nickelate superconductors has attracted substantial attention in the condensed matter physics community and become a rapidly growing frontier in the field of superconductivity¹¹⁻¹⁵. Notably, pressure plays a significant role in regulating the superconductivity of nickelates. It has been shown that the T_c of $\text{Pr}_{0.82}\text{Sr}_{0.18}\text{NiO}_2$ thin films can be significantly increased to ~ 31 K by applying hydrostatic pressure up to 12 GPa¹⁶, though it is still below the McMillan limit. Recent studies have observed signatures of high-temperature superconductivity (HTSC) in pressurized single crystals of $\text{La}_3\text{Ni}_2\text{O}_{7-\delta}$ with an onset T_c of about 78 K, exceeding the McMillan limit and indicating a potential new class of HTSC at liquid nitrogen temperatures¹. In the original work, although a sharp drop in resistance was observed, zero-resistance state was not achieved. Later researches achieved zero-resistance state under improved hydrostatic pressure conditions^{2,3,9}, while the detection of the Meissner effect — a key property of superconductivity — remains a challenge due to the poor superconducting volume fraction and limited magnetic measurement techniques under high pressure conditions. Zhou *et al.* conducted modulated a.c. susceptibility measurements on pressurized $\text{La}_3\text{Ni}_2\text{O}_{7-\delta}$ single crystals and found a faint diamagnetic response, suggesting a filamentary nature of the observed superconductivity with an estimated superconducting volume fraction of only about 1%¹⁰. Currently, it remains under debate whether bulk HTSC can be achieved in pressurized $\text{La}_3\text{Ni}_2\text{O}_{7-\delta}$.

Recently, Pr-substituted $\text{La}_2\text{PrNi}_2\text{O}_7$ polycrystalline samples with improved quality were synthesized and shown to achieve bulk HTSC with $T_c^{\text{zero}} \sim 60$ K and superconducting shielding volume fraction $f_{\text{sc}} \geq 97\%$ at 19 GPa via a.c. magnetic susceptibility measurements¹⁷. However, the diamagnetic response observed in the a.c. measurement is not sufficient to prove the Meissner effect, since the diamagnetism resulting from the shielding effect can also occur in other situations, e.g. perfect conductors. In the case of Ruddlesden-Popper (R-P) nickelate superconductors, there is no clear evidence of the Meissner effect, which should be characterized by the magnetic field

expulsion during field cooling (FC) process. Meanwhile, multislice electron ptychography (MEP) and angle-resolved photoemission spectroscopy (ARPES) studies at ambient pressure on $\text{La}_3\text{Ni}_2\text{O}_{7-\delta}$ suggest obvious inhomogeneity⁵⁻⁷, which calls for spatially resolved methods to investigate the HTSC feature of nickelate superconductors. Due to its high sensitivity, high spatial resolution and especially its compatibility with diamond anvil cells (DACs), quantum sensing with nitrogen-vacancy (NV) centers in diamond has proven to be a unique tool for studying magnetic properties under high pressure¹⁸⁻²³, which provides a great opportunity to verify the Meissner effect in bilayer nickelates and to determine the distribution of superconductivity under high pressure.

In this work, shallow NV centers in [111]-crystal cut anvils are used as in-situ quantum sensors to investigate the Meissner effect in pressurized bilayer nickelates $\text{La}_3\text{Ni}_2\text{O}_{7-\delta}$ and $\text{La}_2\text{PrNi}_2\text{O}_7$. Unambiguous magnetic field expulsion effect is observed in both zero field cooling-field warming (ZFC-FW) and FC measurements, which is a solid signature of the Meissner effect. Comparative experiments on different pressure transmitting media (silicone oil and KBr) and nickelates ($\text{La}_3\text{Ni}_2\text{O}_{7-\delta}$ and $\text{La}_2\text{PrNi}_2\text{O}_7$) reveal that an improved hydrostatic pressure condition and the substitution of La by Pr in $\text{La}_3\text{Ni}_2\text{O}_{7-\delta}$ can immensely increase the superconductivity. The correlated measurements of Raman spectra and NV-based magnetic imaging indicate an incomplete structural transformation related to the displacement of oxygen ions emerging in the non-superconducting region. Our results provide crucial evidence for the Meissner effect and contribute to a deeper understanding of the mechanism of HTSC in pressurized bilayer nickelate superconductors.

Results and discussions

As shown in Fig. 1a, the high-pressure sample chamber consists of two diamond anvils and a gasket. Through the transparent diamond window, optically detected magnetic resonance (ODMR) and Raman spectra can be measured under high pressure, in a correlated manner. To investigate the magnetic field and stress distribution around the superconducting samples, shallow NV centers are created on one of the diamond culets by nitrogen ion implantation (20 keV , $2 \times 10^{14} \text{ cm}^{-2}$) and subsequent high temperature annealing. The spin resonance frequencies of an NV center are

sensitive to the local magnetic field (and also to pressure, temperature and so on) and can be read out optically, providing a convenient and efficient method to study magnetic properties inside DACs. Details of the ODMR technique can be found in the methods and previous works^{20,24}. In this way, we can detect the magnetic flux expulsion of sample during FC process, which is a rather intrinsic property of the Meissner effect in superconductors, and can be used to distinguish between a perfect conductor and a superconductor, as shown in Fig. 1b.

The Meissner effect of $\text{La}_2\text{PrNi}_2\text{O}_7$ and $\text{La}_3\text{Ni}_2\text{O}_{7-\delta}$ polycrystalline samples was studied using diamond quantum sensors, in conjunction with in-situ Raman measurements. For sample A, $\text{La}_2\text{PrNi}_2\text{O}_7$ in liquid pressure transmitting medium (silicon oil), ODMR spectra were measured under different pressures and external magnetic fields. We also performed experiments with $\text{La}_2\text{PrNi}_2\text{O}_7$ (sample B) in a solid pressure transmitting medium (KBr) to investigate the influence of hydrostatic pressure conditions on superconductivity. Correlated Raman and ODMR measurements were performed on sample B to determine the structural distinctions on both the superconducting and non-superconducting regions. Finally, sample C, $\text{La}_3\text{Ni}_2\text{O}_{7-\delta}$ in silicon oil, was measured to investigate the influence of the Pr substitution on the superconducting volume fraction.

Local diamagnetism in $\text{La}_2\text{PrNi}_2\text{O}_7$

We start with the sample of $\text{La}_2\text{PrNi}_2\text{O}_7$ in silicon oil (sample A) at 20 GPa. As shown in Fig. 1c and Fig. 2a, the sample edge and its relative position on the diamond culets were determined by comparing the bright field image and confocal NV fluorescence image. Fig. 2b shows typical ODMR spectra of NV centers near the sample. These spectra were measured under an external magnetic field of around 120 G after zero-field cooling the sample to 6 K. The strength of the external magnetic field was calibrated using the ODMR splitting of the NV centers away from the sample (point A0 in Fig. 2a). For NV centers directly above the sample, e.g. at point A1, the ODMR splitting (644.1 MHz) is noticeably smaller than that of the reference point (672.9 MHz), indicating local diamagnetism of the $\text{La}_2\text{PrNi}_2\text{O}_7$ sample. At the same time, a relatively larger splitting (678.0 MHz) was observed at point A2, which was due to the magnetic flux concentration at the sample edge. By measuring more points around the sample, a superconducting region can be extracted, as shown by the blue color in Fig. 2c. For the measured region of $110 \mu\text{m} * 74.5 \mu\text{m}$, about $2/5$ of the points show diamagnetism, indicating a relatively large fraction of

superconducting shielding volume in the $\text{La}_2\text{PrNi}_2\text{O}_7$ sample.

To verify the Meissner effect of the $\text{La}_2\text{PrNi}_2\text{O}_7$ sample, FC and ZFC-FW measurements were performed at different magnetic fields. Fig. 2d shows the diamagnetism (at point A1) and the flux concentration effects (at point A2) under different external magnetic fields, which show an almost linear dependence in all measured magnetic fields. Following this, ODMR measurements were performed during ZFC-FW and FC processes, with the external magnetic field of 120 G. The detailed experimental protocol is shown in Fig. 2e. As displayed in the Fig. 2f, both the diamagnetism (at point A1) and the flux concentration (at point A2) show clear temperature dependence. In comparison, the reference point (A0) maintains nearly constant ODMR splitting throughout the ZFC-FW and FC processes. From these results, a superconducting transition temperature $T_c \sim 60$ K is obtained and the expulsion of magnetic flux throughout the FC process, an intrinsic property of the Meissner effect, is observed. Meanwhile, compared to the ZFC-FW process, a weaker diamagnetism effect was observed at point A1 during the FC process. This is probably because the external magnetic field can partially penetrate the sample during the FC process, which is a representative signature of type-II superconductors.

To rule out the possibility that the diamagnetism originates from other magnetic impurities, both the ZFC-FW and FC measurements were performed under an external magnetic field of opposite direction and a strength of around -210 G (see Fig. 2e for the experimental protocol). The diamagnetism effect and its temperature dependence are similar to those observed at 120 G (shown in Extended Data Fig. 1b), indicating that the local diamagnetism sensed by the NV centers is not due to the compensating effect of magnetic impurities. In addition, we varied the pressure from 11 GPa to 30 GPa and performed ZFC-FW measurements. The reduced diamagnetic strength at pressures above 20 GPa indicates that superconductivity is gradually suppressed by the pressure (shown in Extended Data Fig. 2a). The T_c determined from the ODMR measurements are included in the phase diagram in Extended Data Fig. 2b. After the pressure decreased to 11 GPa, the effect of diamagnetism disappeared, which is consistent with the electrical resistance results in the previous study¹⁷.

Simultaneous magnetic and Raman measurements

To investigate the effects of pressure transmitting media, another $\text{La}_2\text{PrNi}_2\text{O}_7$ sample (sample B) was loaded in KBr (a solid pressure transmitting medium) and compressed to 30 GPa. We then

characterized the sample with both ODMR and Raman measurements. As shown in Fig. 3a, the confocal image clearly shows the shape and relative position of the sample, the microwave wire, and the edge of the sample chamber. Fig. 3b shows a magnetic field image under an external magnetic field of around 34 G after zero-field cooling the sample to 7 K. Local diamagnetism (reduction of ODMR splitting) was observed in two regions of the sample. The diamagnetic region is noticeably 80% smaller than that in sample A (about 2/5), suggesting improved hydrostatic conditions can significantly increase the superconducting volume fraction.

Fig. 3c shows the temperature dependence of local diamagnetism in sample B during a FW process (under an external magnetic field of around 120 G). As the temperature increases to T_c , the diamagnetic effect gradually fades out. When the temperature is above T_c , the entire region exhibits a uniform magnetic field in line with the strength at reference point B0. More results of the ZFC-FW measurement in sample B can be found in Extended Data Fig. 3a. Compared to sample A, the diamagnetism effect in sample B is smaller. This can be explained by the fact that the liquid pressure transmitting medium (silicon oil) provides better hydrostatic conditions and increases the superconducting volume, so that more pronounced diamagnetism is observed in sample A. These results are consistent with the previous studies on the electrical resistance^{1-3,9}.

Benefited from the high spatial resolution of NV centers, the distribution of the superconducting regions is visually obtained, which allows us to perform targeted spectroscopic measurements. We then used in-situ Raman spectrum to study the structure of pressurized $\text{La}_2\text{PrNi}_2\text{O}_7$ in both the superconducting and non-superconducting regions labeled in Fig. 3b. As shown in Fig. 3d and Extended Data Fig. 3b, a slight difference is observed in the Raman spectra where a satellite peak around 680 cm^{-1} is suppressed in the superconducting region at 20 GPa. The satellite peak is more pronounced in the non-superconducting region and in the sample before compression (see Extended Data Fig. 4a). When the pressure is released to atmospheric pressure, the satellite peak in the superconducting region returns to its original shape. Our density-functional perturbation theory (DFPT) calculations show that structural transformations in $\text{La}_3\text{Ni}_2\text{O}_7$ is manifested as the suppression and degeneracy of Raman peak. As demonstrated in Extend Data Fig. 4b, for the low-pressure $\text{La}_3\text{Ni}_2\text{O}_7$, the three highest Raman-active vibrational modes are B_{1g}^1 , B_{2g} , and B_{1g}^2 , respectively. Along with compressing $\text{La}_3\text{Ni}_2\text{O}_7$ from 0 GPa up to its phase-transition pressure of about 9 GPa, these three modes gradually shift to higher frequencies

and the variance between the B_{2g} and B_{1g}^2 modes becomes increasingly negligible. Indeed, DFPT calculations on the high-pressure show that there is only one Raman-active mode (E_g) above 600 cm^{-1} , which should be attributed to the degeneracy of the B_{2g} and B_{1g}^2 modes. More interestingly, as shown in Extend Data Fig. 4c, we observe the same phenomena in the $\text{Pr}_3\text{Ni}_2\text{O}_7$ case, implying that our discussion above may reflect the common characteristics present in this class of materials. It can be also observed in the bilayer R-P perovskite $\text{Li}_2\text{CaTa}_2\text{O}_7$, which shares a similar structure with $\text{La}_2\text{PrNi}_2\text{O}_7$. The disappearance of the satellite peak in $\text{Li}_2\text{CaTa}_2\text{O}_7$ indicates a structural transformation from a low symmetry phase to a high symmetry phase²⁵. When comparing with the Raman spectra of related compounds²⁶, the satellite peak in $\text{La}_2\text{PrNi}_2\text{O}_7$ is attributed to an oxygen B_{1g} mode. Therefore, the satellite peak in the non-superconducting region can be attributed to the incomplete structural transformation caused by the displacements of the oxygen ions, which is challenging to be observed in X-ray and neutron diffraction²⁷. These results are well consistent with the change of the bond angle of the Ni-O-Ni in $\text{La}_3\text{Ni}_2\text{O}_7$. In the case of $\text{La}_3\text{Ni}_2\text{O}_7$, the emergence of HTSC is along with the structural transformations from *Amam* to *Fmmm* with the change of the bond angle of the Ni-O-Ni and the metallization of the inter-layer σ -bonding bands^{1,6}. Therefore, our results exhibit the structural difference between superconducting and non-superconducting regions and reveal that the inhomogeneous superconductivity originates from the complete and incomplete structural transformations on superconducting and non-superconducting regions in pressurized bilayer nickelate superconductors.

Local diamagnetism and stress imaging in $\text{La}_3\text{Ni}_2\text{O}_{7-\delta}$

To evaluate the effect of Pr substitution in the bilayer nickelate superconductors, a polycrystalline $\text{La}_3\text{Ni}_2\text{O}_{7-\delta}$ sample was loaded with silicon oil as the pressure transmitting medium (sample C). Fig. 4a shows the confocal image of NV fluorescence when the sample is compressed to 20 GPa. Following the experimental protocol shown in Fig. 2e, the ZFC-FW and FC measurements were performed under an external magnetic field of around 120 G. As shown in Fig. 4b, local diamagnetism was observed during both FW and FC processes, confirming the Meissner effect in the $\text{La}_3\text{Ni}_2\text{O}_{7-\delta}$ polycrystalline sample. However, the change of ODMR splitting in sample C is only one-fifth of sample A, indicating that the substitution of La by Pr in $\text{La}_2\text{PrNi}_2\text{O}_7$ can significantly increase the superconducting volume fraction.

Another feature of this sample is that there are obvious differences of ODMR splitting among

different NV centers, even when the temperature is above T_c . This phenomenon can be partly explained by the inhomogeneous distribution of stress. In particular, the compressive stress can shift the center frequency of the ODMR spectra, while the differential stress regulates the ODMR splitting. It is worth noting that this phenomenon also occurs in the former two samples, but the stress effect is much weaker compared to the superconducting diamagnetism effect in the first two samples. Fortunately, NV centers can also serve as in-situ stress sensors. To decouple the contribution of stress, we perform ODMR measurements at 150 K (above T_c) in zero field (see Supplementary Information for details). As shown in Fig. 4c and 4d, the maximum pressure variance among the sample is about 3 GPa. With this in hand, we can eliminate the influence of non-uniform stress distribution and obtain a strain-free magnetism distribution, as shown in Fig. 4e. These differential stress, pressure gradient and the inhomogeneity⁹ could be the reasons of the incomplete structural transformations, leading to the non-superconducting region on the samples.

Finally, the diamagnetism signals of three samples during ZFC-FW are normalized and compared with each other. As shown in Fig. 4f, it can be clearly seen that pressurized $\text{La}_2\text{PrNi}_2\text{O}_7$ in silicon oil exhibits the strongest diamagnetism effect, while $\text{La}_2\text{PrNi}_2\text{O}_7$ in KBr has a relatively weaker signal, indicating that the hydrostatic conditions play an important role in achieving a high superconducting volume fraction. Overall, $\text{La}_3\text{Ni}_2\text{O}_{7.8}$ in silicon oil has the weakest signal, which is consistent with its filamentary nature with a low superconducting volume fraction¹⁰.

Conclusion

In summary, the superconducting Meissner effect is observed in pressurized bilayer nickelate superconductors $\text{La}_3\text{Ni}_2\text{O}_{7.8}$ and $\text{La}_2\text{PrNi}_2\text{O}_7$ using NV center quantum sensors. Magnetic field distribution imaging reveals the differences in superconductivity between these two samples. The substitution of La by Pr in polycrystalline $\text{La}_3\text{Ni}_2\text{O}_{7.8}$ dramatically increases the superconducting volume fraction. ODMR measurements during FC process demonstrate the phenomenon of superconducting magnetic field expulsion, which provides strong evidence for the Meissner effect. By combining ZFC-FW measurements with FC measurements in different external magnetic fields, our results indicate the presence of disorder pinning centers in nickelate high-temperature superconductors, which is a signature of type-II superconductors. Through the correlated

measurement between the ODMR and Raman spectroscopy, we were able to identify the structural difference between superconducting and non-superconducting regions in the $\text{La}_2\text{PrNi}_2\text{O}_7$ sample. These measurements indicate that the inhomogeneous superconductivity originates from the incomplete structural transformations related to the displacement of oxygen ions on the non-superconducting regions and the complete transformations on the superconducting regions, which helps us to understand the underlying mechanism in nickelate high-temperature superconductors.

Our research demonstrates that diamond NV center is a powerful magnetic probe to study inhomogeneous samples under high pressure, due to their high sensitivity and spatial resolution. Using spatially resolved ODMR measurement, we can efficiently perform various in-situ high-pressure experiments, such as Raman and absorption spectroscopy. This approach facilitates a deeper exploration of material properties under extreme high-pressure conditions.

Methods

Sample synthesis. Polycrystalline $\text{La}_2\text{PrNi}_2\text{O}_7$ and $\text{La}_3\text{Ni}_2\text{O}_{7-\delta}$ samples were synthesized using sol-gel method with the identical procedures as described in reference^{3,17}. Stoichiometric mixtures of rare-earth oxides and $\text{Ni}(\text{NO}_3)_2 \cdot 6\text{H}_2\text{O}$ with a purity of 99.99% from Alfa Aesar were dissolved in deionized water together with citric acid and nitric acid. The solution was stirred in a 90 °C water bath for approximately 4 hours, resulting in a vibrant green nitrate gel. The gel was then heat-treated overnight at 800 °C to remove excess organic matter. The product was then ground, pressed into pellets, and sintered in air at 1100-1150 °C for 24 hours.

Sample loading. The pressure is generated using a diamond anvil cell (DAC) made of a non-magnetic BeCu alloy. All experiments are carried out on standard diamond anvils with [111]-crystal cut. These anvils are polished from synthetic type-IIa single crystal diamonds. The diameter of the diamond anvil culet is 300 μm . N ions with an energy of 20 keV and dosage of $2 \times 10^{14} \text{ cm}^{-2}$ are implanted on the diamond culet to create a layer of vacancies. After implantation, the diamond is annealed at 800 °C for 2 hours to form NV centers. A rhenium gasket with an initial thickness of 200 μm is pre-intended to 40 μm , then a 120 μm -diameter hole is drilled in the center with a laser beam. After ultrasonic cleaning, the gasket is coated with a layer of insulating glue

while the hole is covered with a layer of aluminium oxide (Al_2O_3) powder. The aluminium oxide powder is tightly compacted and further drilled to form the high-pressure chamber (with a diameter of about 100 μm). Polycrystalline $\text{La}_2\text{PrNi}_2\text{O}_7$ and $\text{La}_3\text{Ni}_2\text{O}_{7-\delta}$ samples are cut into pieces of 100 $\mu\text{m} \times 60 \mu\text{m} \times 40 \mu\text{m}$ and 40 $\mu\text{m} \times 50 \mu\text{m} \times 30 \mu\text{m}$, respectively, and placed into the chamber. Silicon oil (samples A and C) or KBr disk (sample B) is then loaded into the chamber and serve as the pressure transmitting media. A 0.5- μm thick gold (Au) foil is cut in strips and placed on the diamond to transmit microwave pulses. The Raman spectra of the diamond and the zero-field splitting of NV are used to calibrate the pressure.

ODMR measurement. Optically detected magnetic resonance (ODMR) measurements are performed with a custom-built confocal microscopy system. A 532-nm laser (Changchun New Industries) is used to polarize and read out the spin states of shallow NV centers in the surface layer of the DAC culet. The laser beam is focused on these NV centers through an objective lens with long working distance. The spin-dependent fluorescence emitted by the NV centers is collected by the same objective lens, filtered in the 650-800 nm range, and detected by a single-photon counting module (Excelitas, SPCM-NIR). The counting signal is then recorded and sent to a computer via a data acquisition card (National Instruments, USB-6343). The focus position of the confocal microscopy is controlled by a pair of scanning mirrors, while the focus depth is controlled by a piezo-stage. The laser pulses are generated using an acousto-optic modulator (G&H, AOM), and microwave pulses are controlled by an RF switch (Mini-circuits, ZASW-2-50DRA+). The SPCM, AOM and RF switch are controlled by a programmable multi-channel pulse generator (SpinCore PulseBlasterESR-PRO 500) with temporal resolution down to 2 ns. Some components, including the DAC, objective lens and piezo stage, are housed in a cryostat (Montana Instruments, s100). The samples temperature can be cooled down to 6 K, with a fluctuation of less than 50 mK. The ODMR spectra are recorded in continuous-wave mode, wherein laser excitation, microwave (MW) driving, and photon counting simultaneously performed while the frequency of MW pulses is scanned. Each MW frequency is counted for a duration of 1 ms, evenly divided between signal counts and reference counts when the MW control is switched on or off. This sequence is repeated until a reasonable signal-to-noise ratio is achieved, and the counts of each MW frequency are summed up and normalized by their

respective reference counts. In this way, we can effectively eliminate slow fluctuations caused by laser power instability (< 1%) and sample position drift.

Raman measurement. In-situ high pressure Raman spectrum was performed with a backscattering configuration using a Jobin Yvon HR-Evolution system consisting of a diode-pumped solid state 785-nm laser. The excitation laser beam was focused into a spot of ~ 5 μm in diameter. The low-temperature high-pressure Raman spectra were collected using an S&I MonoVista CRS+ 750 System equipped with a liquid-nitrogen-cooled charge-coupled device (CCD). A 785 nm laser was used, with a spot size of $1 \sim 2$ μm . The laser power was maintained at a low power (~ 3 mW) to avoid overheating during the measurements.

Theory (DFT) calculations. Density functional theory (DFT) calculations were conducted using the projector-augmented wave (PAW) method, implemented in the Vienna *ab initio* simulation package (VASP)^{28,29}. All calculations utilized the Perdew-Burke-Ernzerhof (PBE) generalized gradient approximation (GGA) exchange-correlation functional³⁰. To correct for the self-interaction error on the Ni species, a rotationally averaged Hubbard U correction of 3 eV was applied³¹. For all calculations, a plane wave energy cutoff of 520 eV, an electronic minimization threshold of 10^{-6} eV, and a k -point grid of $n_{kpoints} \times n_{atoms} > 1000$ were adopted. All DFT calculations in this study were performed without spin-polarization. The vibrational frequencies and mode eigenvectors at the zone center Γ point was computed using the density-functional perturbation theory (DFPT).

Data availability

All data are available from the corresponding authors upon reasonable request. Source data are provided with this paper.

Acknowledgments

This work was supported by the National Key R&D Program of China (Grants Nos. 2021YFA1400300, 2023YFA1608900, 2019YFA0308100), the National Natural Science Foundation of China (Grants Nos. 12375304, 12022509, T2121001), the Beijing Natural Science

Foundation (Grants Nos. Z200009, Z230005), the Innovation Program for Quantum Science and Technology (2023ZD0300600). This work was partially carried out at high-pressure synergetic measurement station of Synergetic Extreme Condition User Facility.

Reference

- 1 Sun, H. *et al.* Signatures of superconductivity near 80 K in a nickelate under high pressure. *Nature* **621**, 493-498 (2023).
- 2 Hou, J. *et al.* Emergence of High-Temperature Superconducting Phase in Pressurized $\text{La}_3\text{Ni}_2\text{O}_7$ Crystals. *Chin. Phys Lett.* **40**, 117302 (2023).
- 3 Wang, G. *et al.* Pressure-Induced Superconductivity In Polycrystalline $\text{La}_3\text{Ni}_2\text{O}_{7-\delta}$. *Phys. Rev. X* **14**, 011040 (2024).
- 4 Zhu, Y. *et al.* Superconductivity in pressurized trilayer $\text{La}_4\text{Ni}_3\text{O}_{10-\delta}$ single crystals. *Nature* **631**, 531-536 (2024).
- 5 Dong, Z. *et al.* Visualization of oxygen vacancies and self-doped ligand holes in $\text{La}_3\text{Ni}_2\text{O}_{7-\delta}$. *Nature* **630**, 847-852 (2024).
- 6 Wang, M., Wen, H.-H., Wu, T., Yao, D.-X. & Xiang, T. Normal and Superconducting Properties of $\text{La}_3\text{Ni}_2\text{O}_7$. *Chin. Phys. Lett.* **41**, 077402 (2024).
- 7 Yang, J. *et al.* Orbital-dependent electron correlation in double-layer nickelate $\text{La}_3\text{Ni}_2\text{O}_7$. *Nat. Commun.* **15**, 4373 (2024).
- 8 Xie, T. *et al.* Strong interlayer magnetic exchange coupling in $\text{La}_3\text{Ni}_2\text{O}_{7-\delta}$ revealed by inelastic neutron scattering. *Sci. Bull.*, (2024).
- 9 Zhang, Y. *et al.* High-temperature superconductivity with zero resistance and strange-metal behaviour in $\text{La}_3\text{Ni}_2\text{O}_{7-\delta}$. *Nat. Phys.* **20**, 1269-1273 (2024).
- 10 Zhou, Y. *et al.* Investigations of key issues on the reproducibility of high- T_c superconductivity emerging from compressed $\text{La}_3\text{Ni}_2\text{O}_7$. Preprint at arxiv.org/abs/2311.12361 (2023).
- 11 Li, D. *et al.* Superconductivity in an infinite-layer nickelate. *Nature* **572**, 624-627, (2019).
- 12 Zeng, S. *et al.* Phase Diagram and Superconducting Dome of Infinite-Layer $\text{Nd}_{1-x}\text{Sr}_x\text{NiO}_2$ thin films. *Phys. Rev. Lett.* **125**, 147003 (2020).
- 13 Zeng, S. *et al.* Superconductivity in infinite-layer nickelate $\text{La}_{1-x}\text{Ca}_x\text{NiO}_2$ thin films. *Sci. Adv.* **8**, 7 (2022).
- 14 Ding, X. *et al.* Critical role of hydrogen for superconductivity in nickelates. *Nature* **615**, 50-55, (2023).
- 15 Osada, M., Wang, B. Y., Lee, K., Li, D. & Hwang, H. Y. Phase diagram of infinite layer praseodymium nickelate $\text{Pr}_{1-x}\text{Sr}_x\text{NiO}_2$ thin films. *Phys. Rev. Mater.* **4**, 121801 (2020).
- 16 Wang, N. N. *et al.* Pressure-induced monotonic enhancement of T_c to over 30 K in superconducting $\text{Pr}_{0.82}\text{Sr}_{0.18}\text{NiO}_2$ thin films. *Nat. Commun.* **13**, 4367 (2022).
- 17 Wang, N. *et al.* Bulk high-temperature superconductivity in pressurized tetragonal $\text{La}_2\text{PrNi}_2\text{O}_7$. *Nature* (2024).

- 18 Hsieh, S. *et al.* Imaging stress and magnetism at high pressures using a nanoscale quantum sensor. *Science* **366**, 1349-1354, (2019).
- 19 Lesik, M. *et al.* Magnetic measurements on micrometer-sized samples under high pressure using designed NV centers. *Science* **366**, 1359-1362, (2019).
- 20 Shang, Y.-X. *et al.* Magnetic Sensing inside a Diamond Anvil Cell via Nitrogen-Vacancy Center Spins*. *Chin. Phys. Lett.* **36**, 086201 (2019).
- 21 Yip, K. Y. *et al.* Measuring magnetic field texture in correlated electron systems under extreme conditions. *Science* **366**, 1355-1359, (2019).
- 22 Bhattacharyya, P. *et al.* Imaging the Meissner effect in hydride superconductors using quantum sensors. *Nature* **627**, 73-79, (2024).
- 23 Mengqi Wang *et al.* Imaging magnetism evolution of magnetite to megabar pressure range with quantum sensors in diamond anvil cell. Preprint at arxiv.org/abs/2306.07840 (2023).
- 24 Dai, J.-H. *et al.* Optically Detected Magnetic Resonance of Diamond Nitrogen-Vacancy Centers under Megabar Pressures. *Chin. Phys. Lett.* **39**, 117601 (2022).
- 25 Galven, C. *et al.* Phase Transitions in the Ruddlesden–Popper Phase $\text{Li}_2\text{CaTa}_2\text{O}_7$: X-ray and Neutron Powder Thermodiffraction, TEM, Raman, and SHG Experiments. *Inorg. Chem.* **55**, 2309-2323, (2016).
- 26 Dias, A., Viegas, J. I. & Moreira, R. L. Synthesis and μ -Raman scattering of Ruddlesden-Popper ceramics $\text{Sr}_3\text{Ti}_2\text{O}_7$, $\text{SrLa}_2\text{Al}_2\text{O}_7$ and $\text{Sr}_2\text{LaAlTiO}_7$. *J. Alloys and Compd.* **725**, 77-83, (2017).
- 27 Adler, P., Goncharov, A. F., Syassen, K. & Schönherr, E. Optical reflectivity and Raman spectra of Sr_2FeO_4 under pressure. *Phys. Rev. B* **50**, 11396-11402, (1994).
- 28 Kresse, G. & Furthmüller, J. Efficiency of ab-initio total energy calculations for metals and semiconductors using a plane-wave basis set. *Comp. Mater. Sci.* **6**, 15-50, (1996).
- 29 Kresse, G. & Joubert, D. From ultrasoft pseudopotentials to the projector augmented-wave method. *Phys. Rev. B* **59**, 1758-1775, (1999).
- 30 Perdew, J. P., Burke, K. & Ernzerhof, M. Generalized gradient approximation made simple. *Phys. Rev. Lett.* **77**, 3865-3868, (1996).
- 31 Dudarev, S. L., Botton, G. A., Savrasov, S. Y., Humphreys, C. J. & Sutton, A. P. Electron-energy-loss spectra and the structural stability of nickel oxide: An LSDA+U study. *Phys. Rev. B* **57**, 1505-1509, (1998).

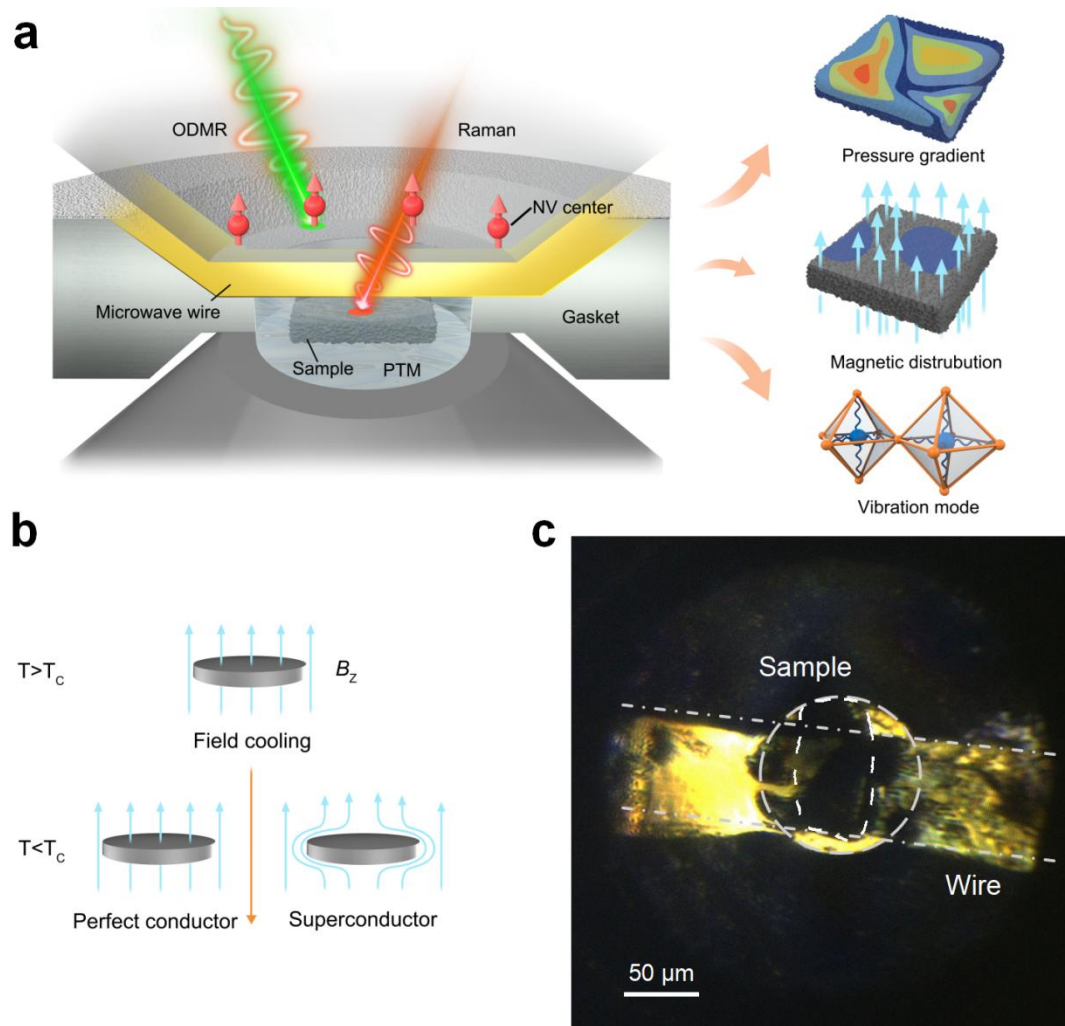


Fig. 1 Correlated characterization of $\text{La}_3\text{Ni}_2\text{O}_{7-\delta}$ in diamond anvil cells (DACs). (a) The $\text{La}_3\text{Ni}_2\text{O}_{7-\delta}$ and $\text{La}_2\text{PrNi}_2\text{O}_7$ samples are wrapped in the pressure transmitting medium (silicone oil or KBr) inside the DAC sample chamber. Correlated measurements of NV-based quantum sensing and Raman spectra are performed to reveal the pressure gradient, magnetic distribution and vibration mode of the samples. This provides a direct method to study the Meissner effect of superconductors under pressure. For in-situ magnetic field and pressure measurement, diamond anvils ([111]-crystal cut) with a layer of shallow NV centers are used, and a gold antenna is placed between the anvil culet and the pressure transmitting medium to transmit the microwave signal. (b) Schematic diagram of the difference between a perfect conductor and a superconductor under field cooling (FC). When $T < T_c$, the superconductor exhibits a magnetic flux expulsion, while the perfect conductor does not. This phenomenon can only be detected in d.c. magnetic measurement. (c) Bright field image of the diamond culet in experiment A at 20 GPa. The sample is outlined by a white dashed line.

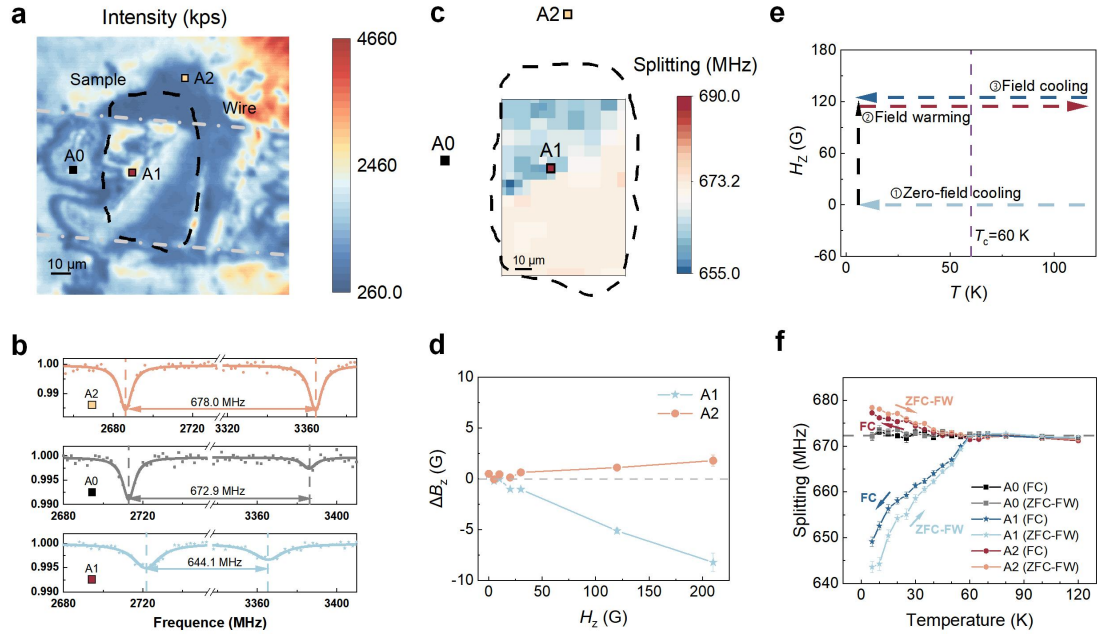


Fig. 2 Local diamagnetism in $\text{La}_2\text{PrNi}_2\text{O}_7$ at 20 GPa. (a) Fluorescence image of sample A ($\text{La}_2\text{PrNi}_2\text{O}_7$ in silicon oil). The edge of the sample is outlined with a black dashed line. (b-c) Typical ODMR spectra of the NV centers (b) and magnetic field image (c) under an external magnetic field of $H_z \sim 120$ G after zero-field cooling of the sample to 7 K. Three points (A0, A1, A2) are selected based on their position with respect to the $\text{La}_2\text{PrNi}_2\text{O}_7$ sample. Point A1 is directly on the sample, A2 is at the edge of the sample and A0 is far away from the sample (serves as a reference point). The blue area in (c) shows the local diamagnetism (these points have a smaller ODMR splitting than that of the reference point). (d) Local magnetic field at the NV positions as a function of the applied external magnetic field (after zero-field cooling). For the NV centers at point A1, their local magnetic field is about 5% smaller than the applied external magnetic field. In sharp contrast, the NV centers at point A2 feel an enhanced local magnetic field. (e) Measurement protocol of field warming after zero-field cooling (ZFC-FW) and field cooling. (f) ODMR splittings of three selected points under 120 G ZFC-FW and FC measurements. The combination of the ZFC-FW and FC curves provide a clear evidence of the Meissner effect.

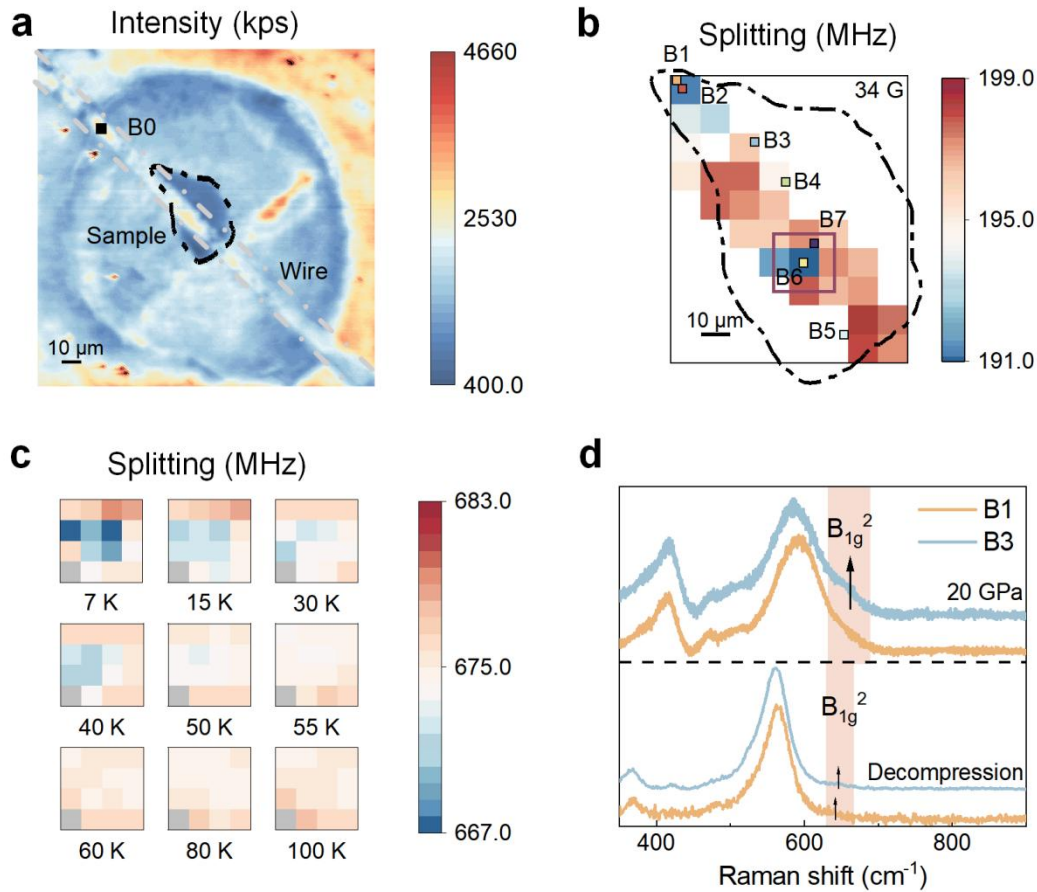


Fig. 3 Correlated magnetic and Raman measurements of $\text{La}_2\text{PrNi}_2\text{O}_7$ under pressure. (a) Fluorescence image of sample B ($\text{La}_2\text{PrNi}_2\text{O}_7$ in KBr). The edge of the sample is outlined with a black dashed line. (b) Magnetic field image under an external magnetic field of $H_z \sim 34$ G after zero-field cooling of the sample to 7 K. The blue region exhibits a noticeable diamagnetism. In-situ Raman measurements are performed on the superconducting regions (B1, B2, B4) and the non-superconducting regions (B3, B5) under different pressures. (c) Magnetic field mapping of one of the superconducting regions (position of purple square marked in b) during the FW process, the external magnetic field is around 120 G. Above the critical temperature T_c , the local diamagnetism disappears and all NV centers feel the uniform external magnetic field. The region on the gray square shows a feeble contrast to fit the ODMR splitting. (d) The Raman spectrum of B1 and B3 at 20 GPa (upper part) and 0 GPa (pressure decompressed, lower part). As shown in the upper part of the figure, a small satellite peak is observed in the non-superconducting region (B3) at 20 GPa, while it is suppressed in the superconducting region (B1). This peak is also presented at atmospheric pressure before compression (shown in Extend Data Fig. 4a). The bottom part of the figure shows the situation after decompression, where the satellite peak recovers in both regions.

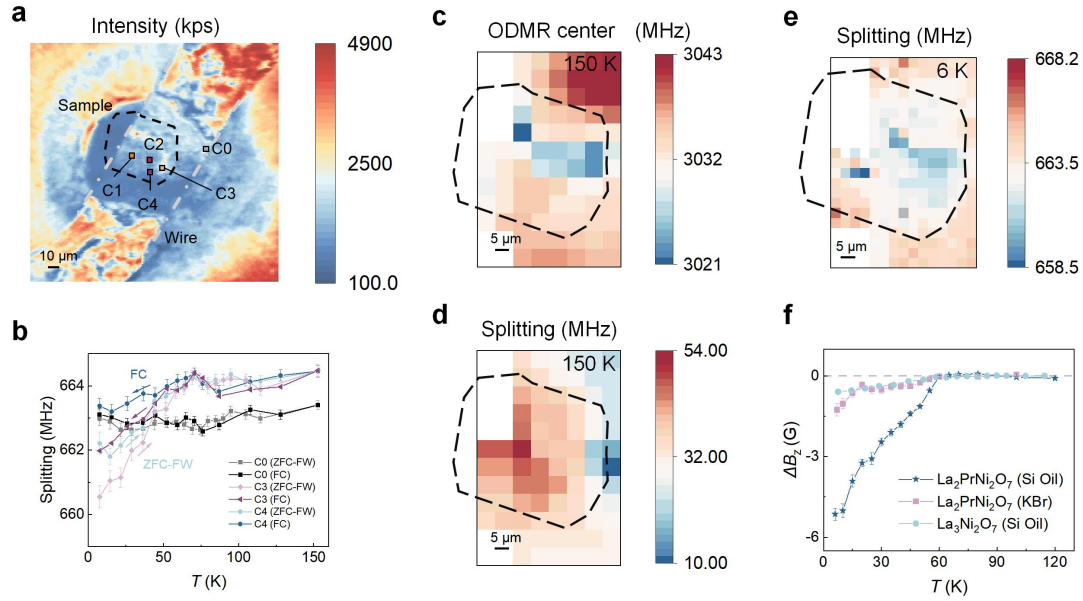
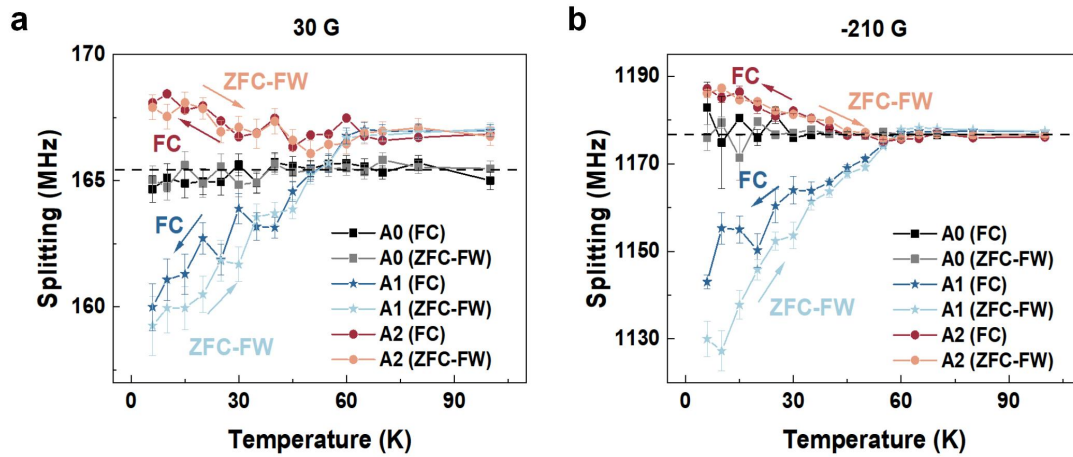
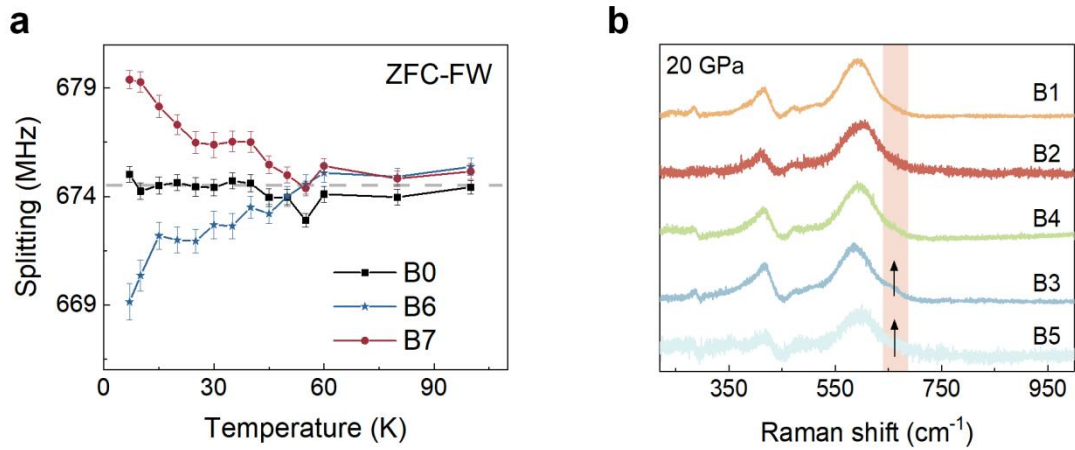


Fig. 4 Magnetic and stress measurement of the $\text{La}_3\text{Ni}_2\text{O}_{7-\delta}$ sample at 20 GPa. (a) Fluorescence image of sample C ($\text{La}_3\text{Ni}_2\text{O}_{7-\delta}$ in silicon oil). The edge of the sample is outlined by the black dashed line. (b) ODMR splitting of the NV centers during the ZFC-FW and FC processes, with an external magnetic field of around 120 G. The NV positions are marked in (a). Both the diamagnetism of the $\text{La}_3\text{Ni}_2\text{O}_{7-\delta}$ sample and the local stress contribute to the ODMR splitting. (c-d) Stress distribution revealed by the zero-field ODMR spectra at 150 K ($> T_c$). The center frequency of the ODMR spectra (e) reveals the compressive stress, while the splitting of the ODMR spectra (d) is proportional to the differential stress. (e) Magnetic image under an external magnetic field of around 120 G after zero-field cooling. Note that the contribution of the stress distribution has been subtracted by the results shown in (c-d). The region on the gray square is an odd point and is therefore not included in the discussion. (f) Comparison of the diamagnetism effect of the three samples during the ZFW-FW measurement. The external magnetic field is around 120 G. For each point, the ODMR splitting at high temperatures ($> T_c$) is used as the reference to calculate ΔB_z .

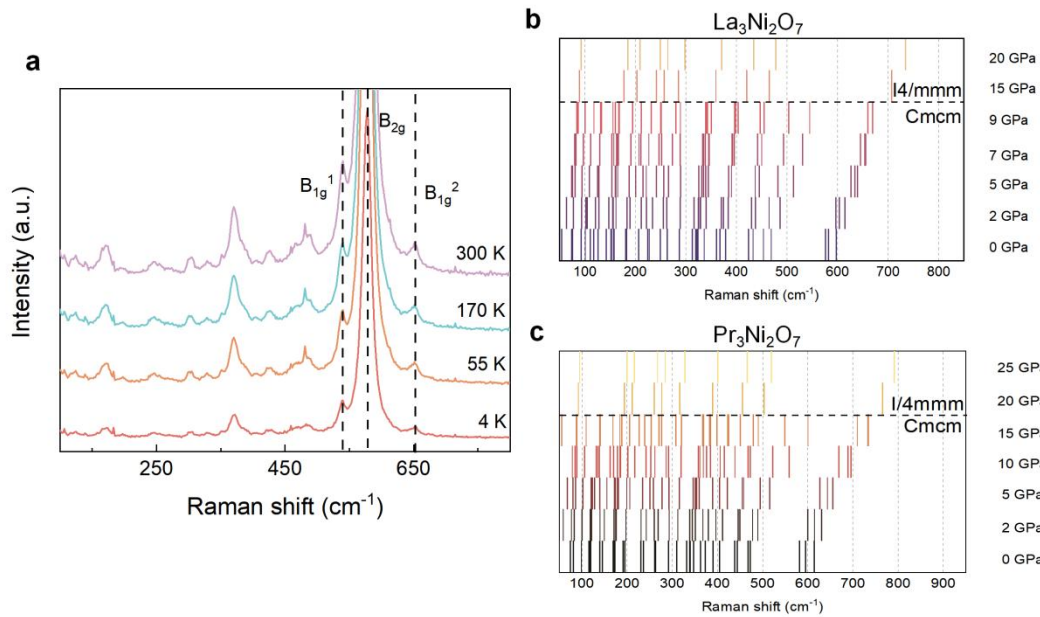


Extended Data Fig. 1 Diamagnetism of sample A ($\text{La}_2\text{PrNi}_2\text{O}_7$ in silicon oil) under different external magnetic fields. ODMR splitting during the ZFC-FW and FC processes of sample A at 20 GPa and an external magnetic field of 30 G (**a**) and -210 G (**b**). The measured points (A0, A1 and A2) are marked in Fig. 2 (a) and the measurement protocol is shown in Fig. 2e. The ODMR splitting of FC is close to the splitting of ZFC-FW at 30 G, while the ODMR splitting of FC is smaller than that of ZFC-FW at -210 G. This agrees well with the magnetic behavior in superconductors with disorder pin: When the external magnetic field becomes larger, more magnetic flux can penetrate through the superconductor, which makes a difference between the diamagnetism during the ZFC-FW and FC processes. The larger the external magnetic field, the more magnetic fluxes can penetrate the superconductor.



Extended Data Fig. 3 Diamagnetism and Raman spectra of sample B ($\text{La}_2\text{PrNi}_2\text{O}_7$ in KBr) (a)

ODMR measurement at test points at 30 GPa during the ZFC-FW process. **(b)** Raman spectra measured at the test points of sample B at 20 GPa. The position of the test points is shown in Fig. 3b. Points B1, B2 and B4 are located on the superconducting region, B3 and B5 on the non-superconducting region. A satellite peak around 680 cm^{-1} can be found in the Raman spectra of B3 and B5, while it is suppressed in the Raman spectra of B1, B2 and B4.



Extended Data Fig. 4 The Raman spectrum of $\text{La}_2\text{PrNi}_2\text{O}_7$ at ambient pressure and the DFPT calculations results. (a) Typical Raman spectrum measured with a 785 nm laser on the $\text{La}_2\text{PrNi}_2\text{O}_7$ at ambient pressure and temperatures from 4 K to 300 K. The Raman spectrum is evenly distributed over the sample. **(b-c)** The Raman-active modes with increasing pressure of $\text{La}_3\text{Ni}_2\text{O}_7$ **(b)** and $\text{Pr}_3\text{Ni}_2\text{O}_7$ **(c)** from DFPT calculations. The three highest Raman-active vibrational modes B_{1g}^1 , B_{2g} , and B_{1g}^2 are correspondingly shown in **(a)**. With increasing pressure, these three modes gradually shift to higher frequencies and the variance between the B_{2g} and B_{1g}^2 modes becomes negligible. In the high-pressure structure, there is only one Raman-active mode (E_g) above 600 cm^{-1} , which is due to the degeneracy of the B_{2g} and B_{1g}^2 modes.